# Effects Of Simultaneous CO2 Addition To The Fuel And Oxidizer Streams On Soot Formation In Co-flow Diffusion Ethylene Flame

Yu Yang

Shu Zheng

Yuzhen He

Hao Liu

*et. al. For a complete list of authors, see* *https://scholarsmine.mst.edu/mec_aereng_facwork/5398*

### Recommended Citation

Full Length Article

# Effects of simultaneous $CO_2$ addition to the fuel and oxidizer streams on soot formation in co-flow diffusion ethylene flame

Yu Yang [a], Shu Zheng [a,*], Yuzhen He [a], Hao Liu [a], Ran Sui [b], Qiang Lu [a,*]

[a] National Engineering Research Center of New Energy Power Generation, North China Electric Power University, Beijing 102206, China
[b] Department of Mechanical and Aerospace Engineering, Missouri University of Science and Technology, Rolla, MO 65409, USA

## ARTICLE INFO

## ABSTRACT

Soot formation in a co-flow diffusion ethylene flame with the addition of $CO_2$ to the fuel (the $CO_2$-F), oxidizer (the $CO_2$-O), and fuel/oxidizer (the $CO_2$-F/O) streams was numerically and experimentally investigated in this study. The effects of different $CO_2$ addition ways on soot inception, soot condensation, H-abstraction-$C_2H_2$-addition (HACA) and oxidation by $O_2$/OH processes, were quantitatively analyzed by introducing the integrated reaction rates over the whole computational domain. The simulated and experimental results showed that the $CO_2$-F/O was the most effective in inhibiting soot formation and flame temperature, followed by the $CO_2$-O, and the $CO_2$-F. Compared with the $CO_2$-F, the suppression effect of the $CO_2$-O on soot inception was weaker due to the higher concentration of benzo(ghi) fluoranthene (BGHIF). Since the rate of $C_4H_2$ formation via $C_2H_4 \rightarrow C_2H_3 \rightarrow C_2H_2 \rightarrow C_4H_2$ was inhibited by the $CO_2$-O, lowering the consumption rate of acenaphthalene (A2R5) via $C_4H_2$ + A2R5=>A4, more A2R5 converted to BGHIF via A2R5 $\rightarrow$ A2- $\rightarrow$ A2 $\rightarrow$ BGHIF. The suppression effects of different ways of $CO_2$ addition on HACA surface growth and soot condensation were identical: $CO_2$-F < $CO_2$-O < $CO_2$-F/O. The decrease of benzo(a)pyrene (BAPYR) mole fraction accounted for the decline of soot condensation rate, and the decreases of H and OH mole fractions were responsible for the drop of HACA surface growth rate. Compared with the $CO_2$-F, the $CO_2$-O and the $CO_2$-F/O had stronger suppression effects on the soot oxidation by $O_2$ process due to the lower concentration of $O_2$ in the oxidizer stream. Whichever $CO_2$ addition ways were adopted, the soot oxidation by $O_2$ process was more sensitive than the soot oxidation by OH process with the $CO_2$ addition.

## 1. Introduction

Soot emission from hydrocarbon-fuel combustion can cause severe harm to environment and human health [1]. In addition, soot has a strong absorbing ability in visible and near-infrared radiation, which is responsible for the global warming [2]. To reduce pollutant emission in the combustion of hydrocarbon fuels, various technologies have been developed, such as the exhaust gas recirculation (EGR) technology [3] and flue gas recirculation (FGR) technology [4], in which a portion of exhaust gas flows back to engine or burner to decrease the concentration of reactive components and reduce the combustion temperature.

Carbon dioxide ($CO_2$) is the main component in exhaust gas. The effect of $CO_2$ addition on the soot formation in the hydrocarbon-fuel combustion has been extensively investigated in previous studies. It is widely known that the soot formation can be obviously inhibited by the $CO_2$ [5,6]. Du et al. [6] experimentally demonstrated that the $CO_2$

addition to the oxidizer stream ($CO_2$-O) suppressed soot inception via three different effects, namely chemical, dilution and thermal effects. Liu et al. [7] numerically isolated the chemical effect of $CO_2$ on the soot formation by introducing a fictitious $CO_2$, which was chemical inert, to the oxidizer stream in an ethylene co-flow flame. The simulated results revealed that the $CO_2$ suppressed soot formation via $CO_2$ + H = CO + OH, resulted in the increase of the concentration of OH radicals, and thus promoted the oxidation of soot precursors. In addition, the decrease of the concentration of $C_2H_2$ caused by the chemical effect of $CO_2$ was another key factor for the decline of the soot formation rate. Similarly, Oh and Shin [8] observed that the soot volume fraction (SVF) was dramatically decreased by the $CO_2$-O. Wang and Chung [9] comprehensively investigated the effect of the $CO_2$-O on the soot inception, soot condensation and H-abstraction-$C_2H_2$-addition (HACA) surface growth processes, by using a detail soot kinetic model. They found that the reduced concentrations of polycyclic aromatic hydrocarbons (PAHs)

**Table 1**
Experimental and numerical conditions.

| Flame conditions | Fuel stream (mL/min) | | Oxidizer stream (L/min) | | $T_{ad}$ (K) |
|---|---|---|---|---|---|
| | $C_2H_4$ | $CO_2$ | Air | $CO_2$ | |
| Case 1 | 150 | – | 40 | – | 2376.6 |
| Case 2 | 150 | 15 | 40 | – | 2363.4 |
| Case 3 | 150 | – | 40 | 4 | 2207.0 |
| Case 4 | 150 | 15 | 40 | 4 | 2196.2 |
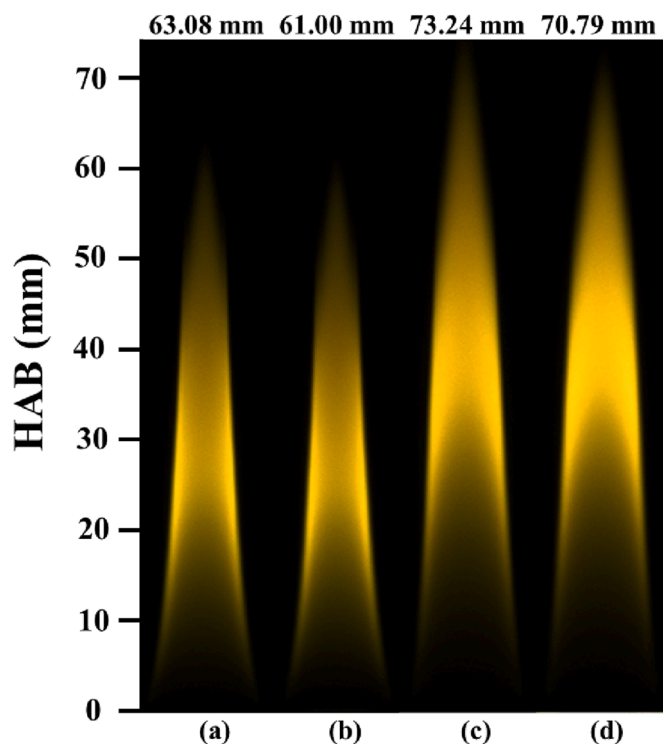


**Fig. 1.** Visible flame images of (a) Case 1, (b) Case 2, (c) Case 3 and (4) Case 4.

accounted for the decrease of soot inception and condensation rates. The addition of $CO_2$ limited H abstraction and $C_2H_2$ generation rates, which consequently lowered the HACA surface growth rate.

Similar to the $CO_2$-O, Gu et al. [10] found that the $CO_2$ addition to the fuel stream ($CO_2$-F) inhibited the soot inception by limiting the PAHs formation and surface growth processes. In addition, it was observed that the soot surface growth was suppressed more than the soot inception. Wu et al. [11] found that the $CO_2$-F not only inhibited the formation of soot/PAHs in ethylene diffusion flame, but also led to a shift in the peak volume fraction from the flame wings to the centerline. However, there was a difference on the suppression between the $CO_2$-F and the $CO_2$-O. The peak SVF decreased by 52.5% from the $CO_2$-F in an ethylene diffusion flame [12], which was remarkably less than the $CO_2$-O (87.2%) [11]. Likewise, Hoerlle and Pereira [13] demonstrated that the $CO_2$-O exhibited a stronger suppression effect on soot formation than the $CO_2$-F. They [13] also concluded that only the chemical effect of the $CO_2$-O dominated the soot suppression, while both thermal and chemical effects were significant for the $CO_2$-F. However, Ashraf et al. [14] experimentally compared the suppressing effects of $CO_2$-F and the $CO_2$-O on soot formation in ethylene diffusion flame. They found that the maximum SVF in the centerline was 0.686 ppm when the $CO_2$ was added to the fuel side, while it was 0.734 ppm when the $CO_2$ was added to the oxidizer side, indicating that the $CO_2$-F exhibited a stronger suppression effect on soot formation than the $CO_2$-O.

Most previous studies were restricted to the effect of the $CO_2$-O or the $CO_2$-F on the soot formation, while the effectiveness of soot suppression among the $CO_2$-F, the $CO_2$-O, and oxidizer/fuel streams ($CO_2$-F/O) were not quantitatively compared and analyzed in their works. It has been demonstrated that the $CO_2$-O had a stronger suppression effect than the $CO_2$-F on soot formation, but no studies compared the effects of three different $CO_2$ addition ways on soot formation, especially on the specific soot formation and oxidation processes, such as soot inception, condensation, HACA surface growth and oxidation by $O_2$/OH processes.

In this study, the effects of the $CO_2$-F, the $CO_2$-O and the $CO_2$-F/O on soot formation characteristics in a co-flow diffusion ethylene flame were numerically and experimentally studied at atmospheric pressure. The distributions of SVF and flame temperature were reconstructed using Abel inverse method based on the radiative intensity of the Red (R) and Green (G) bands measured by a CMOS camera. The co-flow diffusion ethylene flames were modeled using gas reaction mechanisms and a detailed soot sectional model. A novel contribution of this paper is to quantitatively compare the effects of different CO2 addition on detailed soot formation and oxidation processes, including the soot inception, soot condensation, HACA surface growth and oxidation by $O_2$/OH processes. The key factors for different $CO_2$ addition ways on different
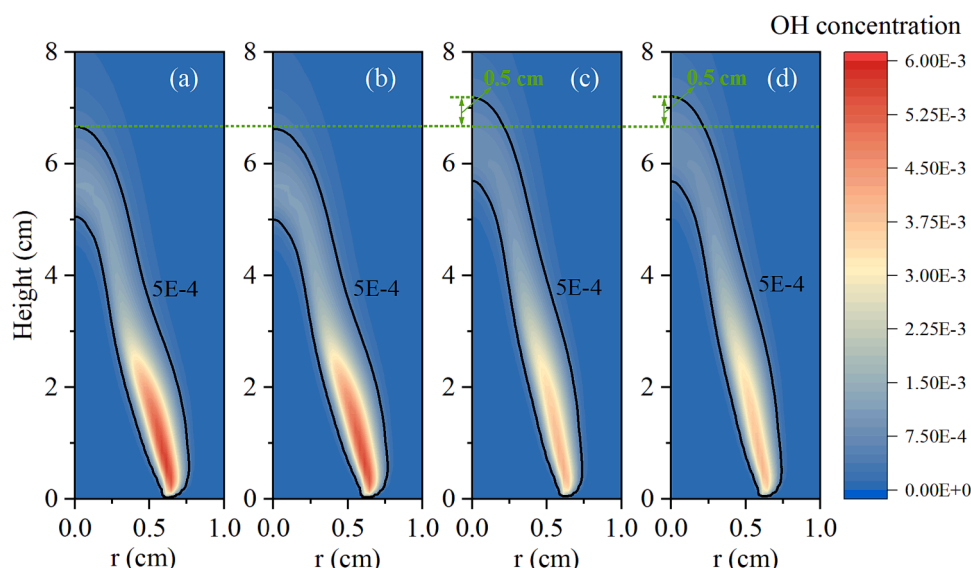


**Fig. 2.** The modeling concentration of OH radical in (a) Case 1, (b) Case 2, (c) Case 3, and (d) Case 4.
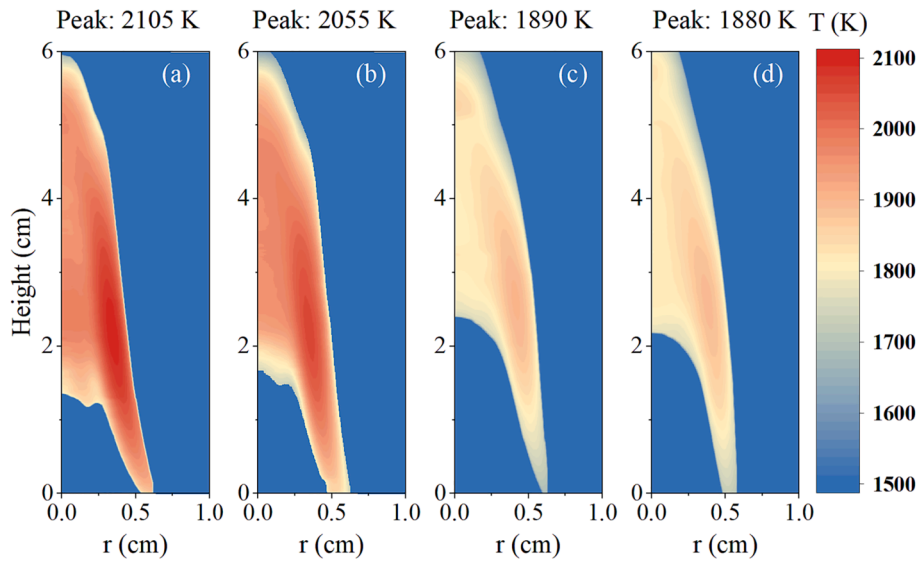
**Fig. 3.** The distributions of measured flame temperatures in (a) Case 1, (b) Case 2, (c) Case 3, and (d) Case 4.
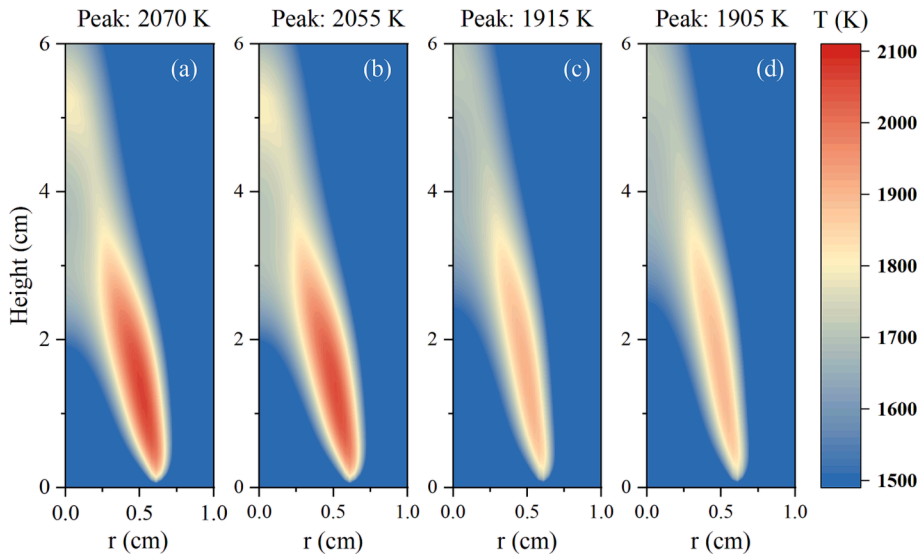


**Fig. 4.** The distributions of simulated flame temperatures in (a) Case 1, (b) Case 2, (c) Case 3, and (d) Case 4.

soot formation and oxidation processes were confirmed based on the integrated reaction rates over the whole computational domain. In addition, the detailed influence pathways of different $CO_2$ addition ways on soot formation precursors, such as benzene and five-rings PAHs, were comparatively analyzed.

## 2. Methods

### 2.1. Experimental methods

A Gülder type burner [15] was used to generate co-flow diffusion ethylene flame. Four different cases were investigated in this work and the flow rates of fuel and oxidizers in each case were summarized in Table 1. The electronic volume flow controllers were used to control the flow rates of gases, and the measurement error was ±1%. The inlet fuel and oxidizer temperatures were both 298 K.

The distributions of flame temperature and SVF were reconstructed by the flame image processing technology. A CMOS camera (Type: Alvium 1800U-040c) with 728 × 544 pixels was used to obtain the R and G data of the flame images. With optically thin assumption, the spectral radiation intensity received by the $j$th pixels can be written as:

$$I_\lambda(j) = \int_{l_0(j)}^{l_i(j)} \kappa_\lambda(l) I_{b\lambda}(l) dl = \int_{l_0(j)}^{l_i(j)} H_\lambda(l) dl \qquad (1)$$

where $l$ was the path of the radiation intensity, $H$ the emission source term, $I_{b\lambda}$ the blackbody radiation intensity of soot, which can be written as:

$$I_{b\lambda} = \frac{c_1}{\lambda^5 (e^{c_2/\lambda T} - 1)\pi} \qquad (2)$$

where $c_1$ and $c_2$ were the Plank's constants. According to Eq. (1) and (2), and the absorption coefficient of soot in the red and green wavelengths was assumed to be the same, the flame temperature can be calculated by dividing the $H$ of red and green wavelengths:

$$T = c_2 \left( \frac{1}{\lambda_G} - \frac{1}{\lambda_R} \right) \ln \left( \frac{\lambda_R^5}{\lambda_G^5} \frac{H_R}{H_G} \right) \qquad (3)$$

Once $T$ was calculated, the absorption coefficient of soot $\kappa_\lambda$ can be
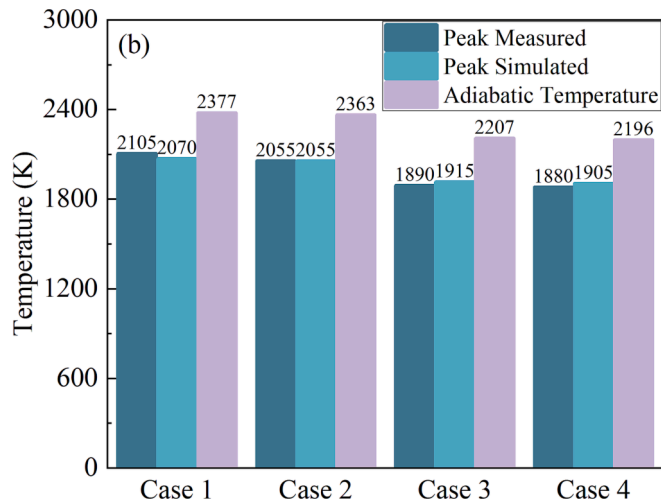
**Fig. 5.** The comparisons of simulated and measured temperatures and adiabatic temperatures in Cases 1–4.
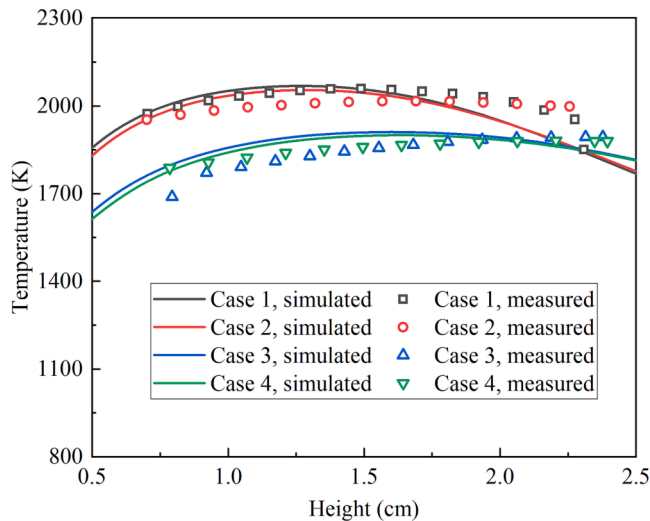


**Fig. 6.** Comparison of measured and simulated temperature profiles along the axial direction at r = 0.43 cm for Case 1 ∼ 4. For experimental results.

obtained from Eq. (1). Finally, the SVF can be obtained according to the relationships between $\kappa_\lambda$ and SVF [16]:

$$\kappa_\lambda = 6\pi E(m) f_v / \lambda \tag{4}$$

where $f_v$ was the SVF and $E(m)$ was a function of the complex refractive index $m$, defined as:

$$E(m) = \frac{6nk}{(n^2 - k^2 + 2)2 + 4n^2 k^2} \tag{5}$$

where $n$ and $k$ were the real and imaginary parts of the complex refractive index $m$, respectively, which can be written as [17]:

$$\begin{cases} n = 1.811 + 0.1263\ln\lambda + 0.0207\ln^2\lambda + 0.0417\ln^3\lambda \\ k = 0.5821 + 0.1213\ln\lambda + 0.2309\ln^2\lambda - 0.01\ln^3\lambda \end{cases} \tag{6}$$

The relation between the R and G data measured by the CMOS camera and the blackbody radiation intensity in the temperature range of 300 ∼ 1700 ℃ was calibrated by a blackbody furnace (Type: M330).

### 2.2. Numerical methods

The CoFlame code [18] was used to simulate the experimental

ethylene diffusion flame. The chemical reaction mechanism established by Chernov et al. [19] was adopted in this paper. The soot inception process was modeled by the collision between two five-ring PAHs (A5), i.e., benzo(a)pyrene (BAPYR), benzo(ghi) fluoranthene (BGHIF) and secondary benzo(a)pyrenyl (BAPYR*S). The soot condensation process was assumed to be the results of collision of A5s and aggregates with a condensation efficiency of 0.5. The HACA surface growth process was described by the HACA mechanism. The fraction of reactive soot surface sites was assumed to be $[\alpha = \min[0.004\exp(10800/T), 1.0]$ according to Ref. [20].

The radiative heat transfer equation was solved by the discrete ordinates method (DOM) [21]. The radiation emitted by $H_2O$, $CO_2$, CO, and soot was considered in this paper. The statistical narrow-band correlated-$k$ method [22] was used to calculate the radiative properties of gases in the range of 150 ∼ 9300 $cm^{-1}$. The absorption coefficient of soot was calculated by $k_s = 5.5 f_v \eta$.

The numerical domain was 11.5 cm (streamwise, z) × 3.8 cm (radius, r), and was divided into 160 (z) × 80 (r) non-uniform control volumes. The minimum resolution in the streamwise direction was 0.02 cm and in the radius direction was 0.03 cm. All numerical simulations were performed in a 40-core server.

## 3. Results and discussions

### 3.1. Flame appearance

Fig. 1 showed the visible flame appearances in Cases 1 ∼ 4. The visible flame height of Case 1 was 63.08 mm, which was slightly higher than that of 61.00 mm in Case 2, but obviously lower than that of 73.24 mm in Case 3. The numerical flame height was indicated by the OH radical [23]. The modeling concentration of OH radical in Cases 1 ∼ 4 were compared in Fig. 2. It is clear from Fig. 2 that the contour line of OH concentration of 5E-4 in Cases 3 and 4 were about 0.5 cm higher than those in Cases 1 and 2. This is mainly because the $O_2$ concentration was lowered by the $CO_2$-O and the flame ignition was delayed.

### 3.2. Flame temperature

The distributions of simulated and measured flame temperatures in Cases 1–4 were depicted in Figs. 3 and 4. As shown in Fig. 3, the simulated high-temperature regions of Cases 1–4 located in the flame wing region, which were consistent with those in the measured results shown in Fig. 4. The simulated and measured peak temperatures and adiabatic temperatures of Cases 1–4 were compared in Fig. 5. According to Fig. 5, the simulated and measured peak temperatures and adiabatic temperature exhibited the same variation trend in the $CO_2$-F, $CO_2$-O and $CO_2$-F/O. Compared with the measured results, the maximum relative error of the simulated peak temperature in Cases 1 ∼ 4 was around 1.7%. With regard to the $CO_2$-F cases, both the simulated and measured peak temperature decreased to 2055 K, shown in Fig. 3(b) and Fig. 4(b). The measured and simulated peak temperatures and adiabatic temperature decreased by 215 K, 155 K and 170 K in the $CO_2$-O cases, respectively, showing a more suppression effect on the flame temperature in the $CO_2$-O than that in the $CO_2$-F. Compared with the $CO_2$-F and $CO_2$-O, the flame temperature decreased the most in the $CO_2$-F/O. The simulated and measured peak temperatures and adiabatic temperature in the $CO_2$-F/O decreased by 225 K, 165 K and 180 K, respectively.

The measured and simulated temperature profiles along the axial direction at r = 0.43 cm, where the peak tempearture occurred, were compared in Fig. 6. It is clear from Fig. 6 that the simulated temperature for Cases 1 ∼ 4 first increased, then decreased with height increased, which was the same as measured temperature profiles. At height of 0.7 ∼ 1.7 cm, the measured temperatures of Cases 1 and 2 agreed well with the simulated temperatures. For Cases 3 and 4, the simulated temperature profiles were almost consistent with the simulated temperature profiles at height of 1.0 ∼ 2.0 cm.
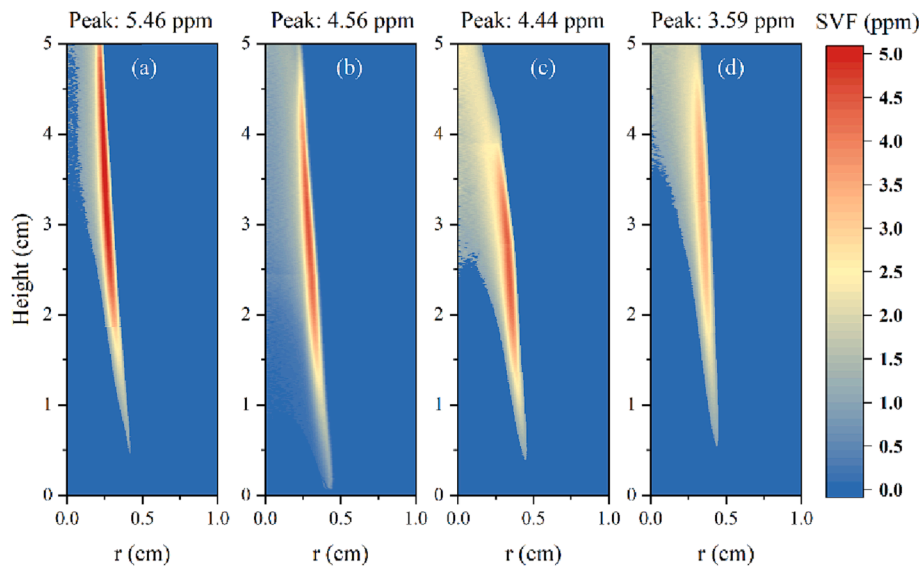
**Fig. 7.** The distributions of measured SVF in (a) Case 1, (b) Case 2, (c) Case 3, and (d) Case 4.
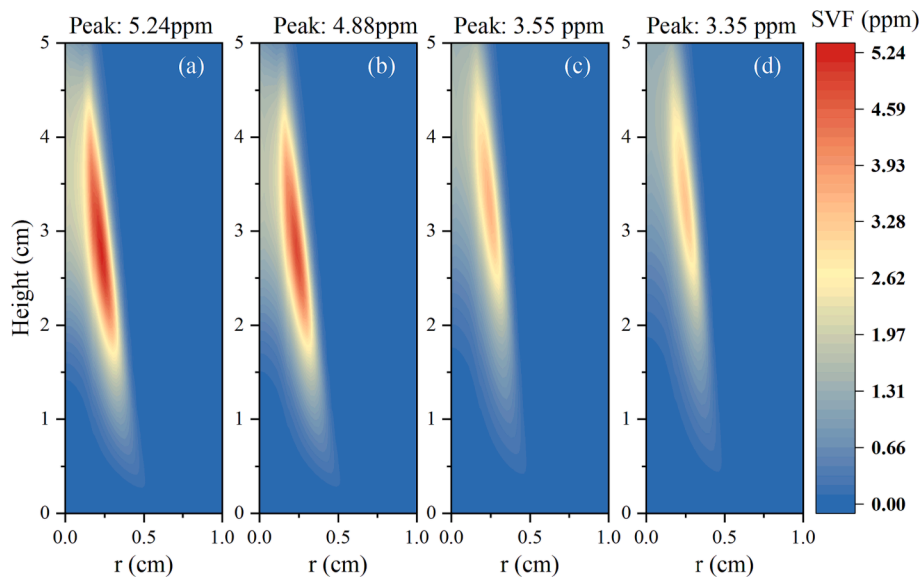


**Fig. 8.** The distributions of simulated SVF in (a) Case 1, (b) Case 2, (c) Case 3, and (d) Case 4.

### 3.3. Soot volume fraction

The simulated and measured SVFs in Cases 1–4 were compared in Figs. 7 and 8. As shown in Fig. 7, the soot predicted in Cases 1–4 was mainly generated in the flame wing region, which agreed well with the measured results shown in Fig. 8. Comparing Fig. 7(a) with 7(b), the peak SVF decreased by 0.9 ppm in the $CO_2$-F. While a larger decrease of 1.02 ppm was observed in the $CO_2$-O (in Fig. 7(a) and (c)). The peak SVF of $CO_2$-F/O decreased by 1.87 ppm in comparison of Fig. 7(a) and (d), indicating that the $CO_2$-F/O had the most inhibiting effect on soot formation. As shown in Fig. 9, the simulated peak SVF in Cases 1–4 captured well with the measured results and showed the same variation trend, demonstrating that the present models could provide good prediction of the experimental SVFs.

In order to quantitatively illustrate how different $CO_2$ addition ways affected soot formation processes at different heights of the flame, the radially integrated rate of each formation process was calculated:

$$\alpha = 2\pi \int_0^r S_{proc} r dr \tag{7}$$

where $S_{proc}$ was the rate of soot inception ($\alpha_{IN}$), soot condensation ($\alpha_{CO}$), HACA surface growth ($\alpha_{HACA}$), and oxidation by $O_2$/OH ($\alpha_{O2}/\alpha_{OH}$) at a given location, and $r$ was the radial position. The distributions of radially integrated soot formation and oxidation rates in Cases 1–4 were plotted in Fig. 10.

As shown in Fig. 10(a), the soot inception process occurred at the lower position of the flame and the peak $\alpha_{IN}$ located at a height of around 0.2 cm. Subsequently, the soot condensation and HACA processes occurred. The peak $\alpha_{CO}$ and $\alpha_{HACA}$ were 2–3 orders of magnitude larger than the peak $\alpha_{IN}$, indicating that the soot condensation and HACA processes played a major role in the increasing SVF. It was clear from Fig. 10(d) and (e) that the peak $\alpha_{O2}$ was about two times larger than the peak $\alpha_{OH}$ in Case 1. These two processes dominated the soot oxidation at different flame height ranges. The soot oxidation by OH process started at the height of 1 cm and the soot oxidation by $O_2$ process started at the
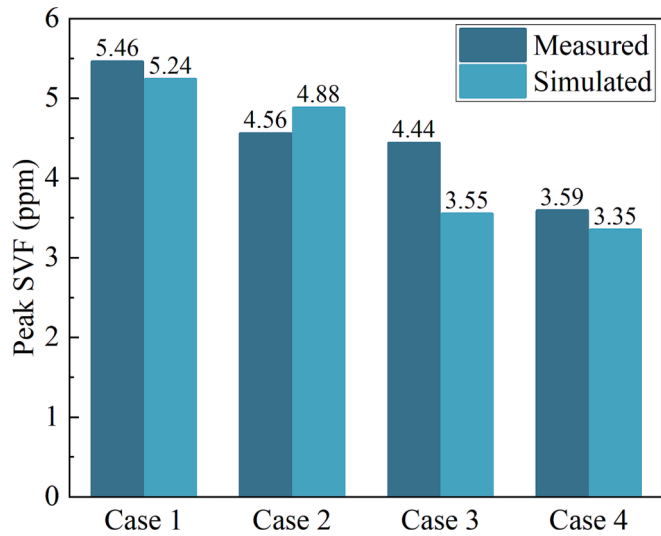
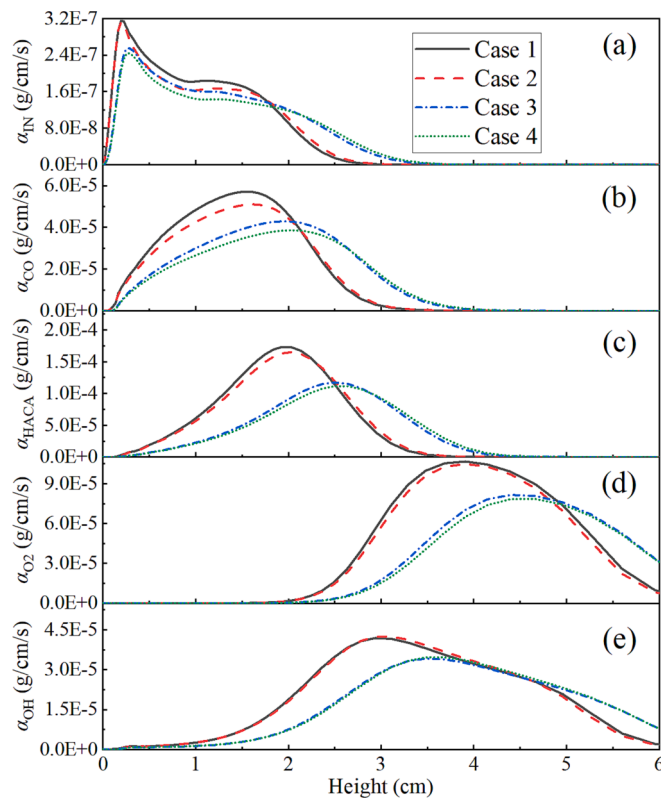**Fig. 9.** The comparisons of simulated and measured peak SVFs.



**Fig. 10.** The axial distributions of radially integrated soot formation and oxidation rates: (a) inception, (b) condensation, (c) HACA, (d) soot oxidation by $O_2$, and (e) soot oxidation by OH in Cases 1–4.

height of 2 cm. Because the OH radicals formed in the flame reaction zone, and it took more time for $O_2$ to transfer from the oxidizer stream to the flame reaction zone. Both the soot oxidation by OH and O2 processes terminated at the height of 6 cm.

As shown in Fig. 10, different $CO_2$ addition ways resulted in considerable discrepancies on each soot formation or oxidation process. In order to further explain how $CO_2$ addition ways impacted soot formation processes, the key factors contributing to the soot inception, soot condensation, HACA surface growth and oxidation by $O_2$/OH processes in Cases 1–4 were comprehensively compared and analyzed in the
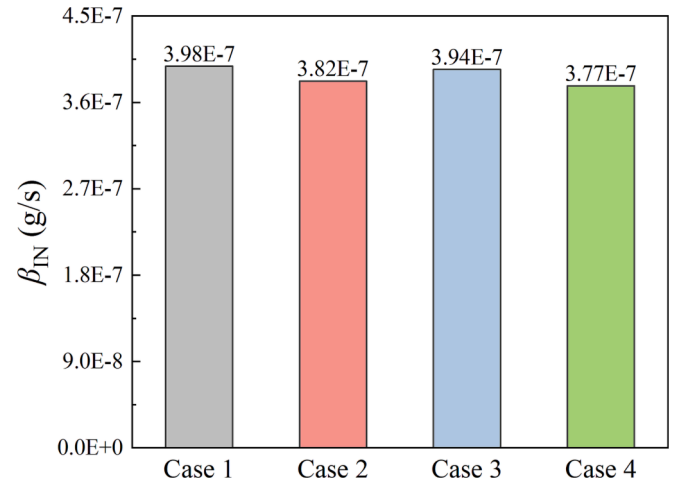


**Fig. 11.** The integrated soot inception rates over the whole computational domain.

following section.

### 3.4. Effect on the soot inception

In Fig. 10(a), $\alpha_{IN}$ of Cases 1 and 2 almost overlapped at the height of $0 \sim 0.2$ cm. As the height increased, the $\alpha_{IN}$ of Case 2 decreased faster than that of Case 1, leading to the lower $\alpha_{IN}$ of Case 2 at the height of 0.3 $\sim 2$ cm. Generally, the soot inception was suppressed by the $CO_2$-F. Likewise, the suppression effect of the $CO_2$-F on soot inception could be found by comparing the $\alpha_{IN}$ of Cases 3 and 4. At the heights of 0–0.2 cm and 1–2 cm, the $\alpha_{IN}$ values of Case 2 were larger than those of Case 3, but opposite at the height over 2 cm. This made it difficult to compare the soot suppression effect between the $CO_2$-F and $CO_2$-O. Hence, the integrated soot inception rate over the whole computational domain ($\beta$, g/s) was introduced:

$$\beta = \int_0^h \alpha dh \tag{8}$$

As shown in Fig. 10(a), although the peak $\alpha_{IN}$ of Case 3 was less than that of Case 2, the $\beta_{IN}$ of Case 3 shown in Fig. 11 was 0.12E-7 g/s larger than that of Case 2, indicating that the $CO_2$-F had more significant suppression effect on the soot inception than the $CO_2$-O. This also demonstrated that it was not comprehensive to adopt the peak $\alpha_{IN}$ to evaluate the suppression effects of different $CO_2$ addition ways on soot inception. The peak $\alpha_{IN}$ and $\beta_{IN}$ in Case 4 were obviously less than those in other cases, which implied that the $CO_2$-F/O had the most suppression effect on the soot inception.

The soot inception was assumed to be the collision of two A5s. Therefore, the soot inception rate mainly depended on the mole fractions of these A5s. Fig. 12(a)-(c) showed the axial distributions of radially integrated mole fractions ($\gamma$, cm$^2$) of three different A5s calculated by:

$$\gamma = 2\pi \int frdr \tag{9}$$

where $f$ was the mole fraction of the specie at a given location.

As shown in Fig. 12(a)-(c), the peak $\gamma_{BAPYR*S}$ values of Cases 1–4 were 4 orders of magnitude less than the peak $\gamma_{BGHIF}$ and $\gamma_{BAPYR}$, indicating that BGHIF and BAPYR were the two major species involving in the soot inception. It was clear from Fig. 12(a) that the axial distributions of $\gamma_{BGHIF}$ of Cases 1–4 were more in line with those of $\alpha_{IN}$ (see Fig. 10(a)) compared with the $\gamma_{BAPYR}$. On the other hand, the peak $\gamma_{BGHIF}$ values of Cases 1–4 were located at the height of around 0.2 cm, which were consistent with the location of peak $\alpha_{IN}$. However, the locations of peak $\gamma_{BAPYR}$ of Cases 1–4 were around 0.3 cm higher than those of peak $\alpha_{IN}$. It
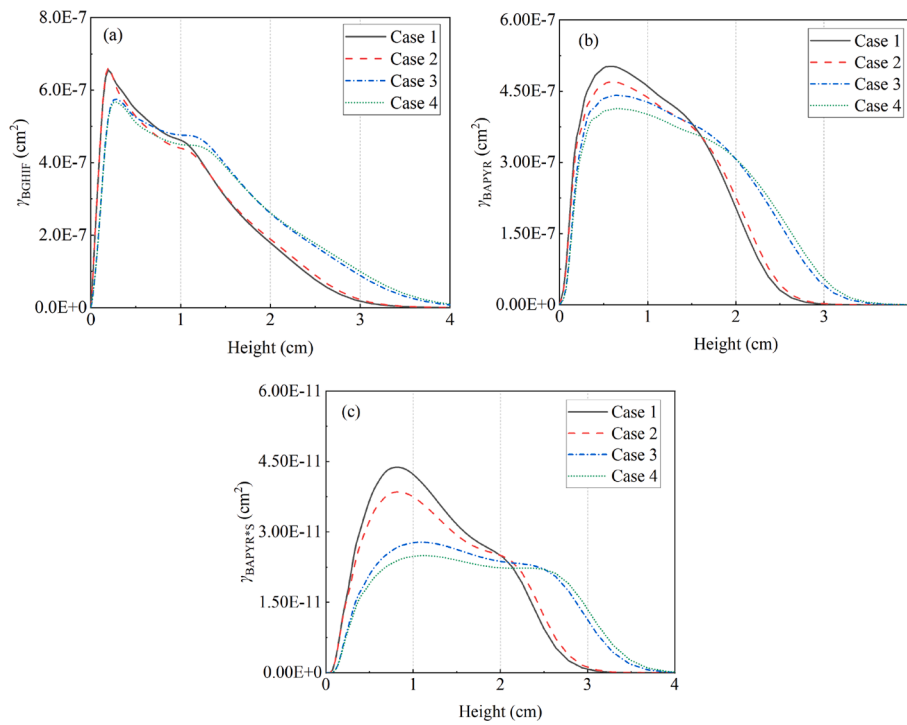
**Fig. 12.** The axial distribution of $\gamma$ of (a) BGHIF, (b) BAPYR, and (c) BAPYR*S.
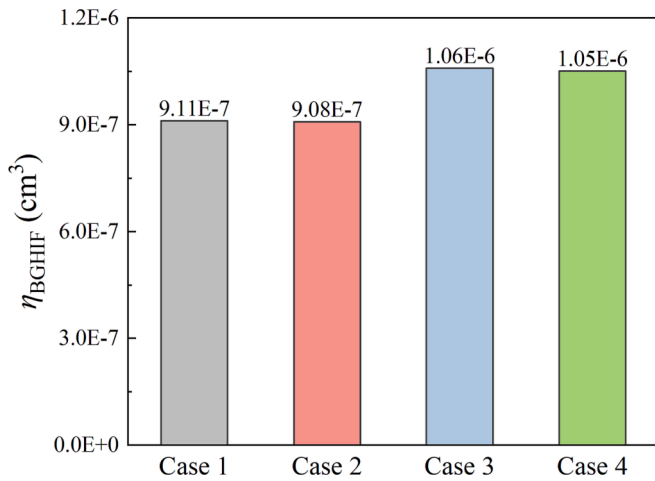


**Fig. 13.** The integrated mole fractions of BGHIF over the whole computational domain.

could thus be concluded that BGHIF dominated in the soot inception.

Similar to the soot inception, it was difficult to distinguish the inhibiting levels of different $CO_2$ addition ways on the BGHIF formation according to the peak $\gamma_{BGHIF}$ shown in Fig. 12(a). Therefore, the integrated mole fraction of BGHIF over the whole computational domain ($\eta$, $cm^3$) was obtained to evaluate the formation rate of BGHIF:

$$\eta = \int_0^h \gamma dh \qquad (10)$$

As shown in Fig. 13, the $\eta_{BGHIF}$ of Case 2 was slightly less than that of Case 1, which demonstrated that the $CO_2$-F had a limited inhibiting effect on the BGHIF formation. It could be found from the Fig. 13 and Fig. 11 that the suppression effect of the $CO_2$-F on $\beta_{IN}$ was stronger than that on $\eta_{BGHIF}$, indicating that the BGHIF was not the only key factor for the soot inception. Besides the concentrations of PAHs, the flame temperature was also a key factor for the soot inception [24]. Compared

with Case 1, the peak temperature of Case 2 decreased by 15 K, which contributed to the decrement of $\beta_{IN}$. The effect of the $CO_2$-O on the $\eta_{BGHIF}$ was contrary to the $CO_2$-F. As shown in Fig. 13, the formation of BGHIF was promoted by the $CO_2$-O and the $\eta_{BGHIF}$ of Case 3 was around 16% larger than that of Case 1. Although the formation of BGHIF was promoted by the $CO_2$-O, the soot inception was inhibited due to the decrease of peak temperature by 155 K in Case 3. Similarly, the decrease of temperature played a key role in the drop of $\beta_{IN}$ in Case 4.

As discussed above, the decrease of temperature was the main reason for the drop of soot inception rates. However, the increases of $\eta_{BGHIF}$ caused by the $CO_2$-O and $CO_2$-F/O also had a significant impact on the soot inception. Compared with the $CO_2$-F (Case 2), the $\beta_{IN}$ of Case 3 was obviously increased due to the higher $\eta_{BGHIF}$ caused by the $CO_2$-O. Moreover, although the peak temperature in Case 4 was 150 K lower than that in Case 2, their $\beta_{IN}$ values were close to each other (3.82E-7 g/s for Case 2 and 3.77E-7 g/s for Case 4) since the $\eta_{BGHIF}$ of Case 4 was 15.6% larger than that of Case 2.

The formation of BGHIF was described by the chemical mechanism. The integrated reaction rates of reactions involved in BGHIF formation ($\delta$, mol/s) were obtained by:

$$\delta = 2\pi \int_0^h \int_0^r S_{rop} r dr dh \qquad (11)$$

where $S_{rop}$ was the reaction rate. The formation pathways of BGHIF of Cases 1–4 were depicted in Fig. 14 based on $\delta$s (available in supplemental materials).

As shown in Fig. 14, the BGHIF was mainly formed via R783 ($C_{18}H_{11}$ + H = BGHIF + $H_2$), R771 (A2R5-+A1=>BGHIF + $H_2$ + H) and R765 (A1C2H + A2-=>BGHIF + $H_2$ + H). The $CO_2$-F/O limited the $\delta$R783 and $\delta$R771 most, followed by the $CO_2$-O, then the $CO_2$-F. All of these BGHIF formation reaction rates were decreased by the $CO_2$-F, leading to the drop of $\eta_{BGHIF}$ in Case 2. Compared with the $CO_2$-F, the $\delta$R765 increased in the $CO_2$-O and $CO_2$-F/O, which were consistent with the changes of $\eta_{BGHIF}$ and confirmed that R765 primarily accounted for the larger $\eta_{BGHIF}$ in Cases 3 and 4.

A2- was the reactant of R765 and the $\eta_{A2-}$ values of four Cases were displayed in Fig. 15(a). It was clear from Fig. 15(a) that more A2- formed
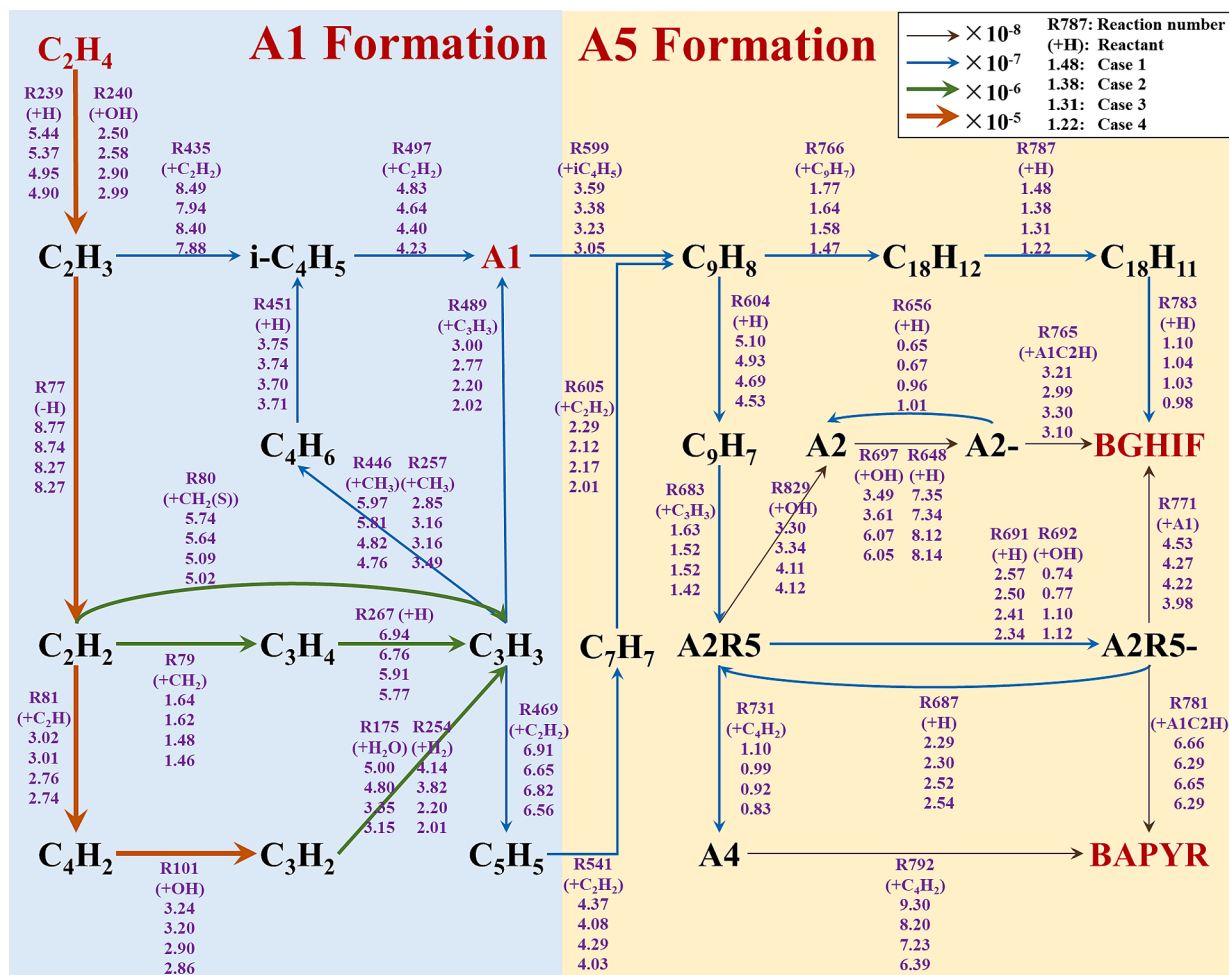
**Fig. 14.** The formation pathways of BGHIF and BAPYR in Cases 1–4.

in the $CO_2$-O, which was the main reason for the increase of $\delta R765$. As shown in Fig. 15(c), the $CO_2$-O resulted in the increase of $\eta_{A2R5}$, which subsequently led to the increase of $\eta_{A2}$ (see Fig. 15(b)) and $\eta_{A2-}$.

Based on Fig. 14, the $\delta R683$ ($C_9H_7 + C_3H_3 = A2R5 + H_2$) decreased by 0.11 mol/s in the $CO_2$-O, which was contrary to the change of $\eta_{A2R5}$. There were four channels competing for A2R5: R829 (A2R5 + OH=>A2 + HCCO), R691 (A2R5 + H = A2R5-+H2), R692 (A2R5 + OH = A2R5-+H2O), and R731 ($C_4H_2$ + A2R5=>A4). As shown in Fig. 15(h), compared with Case 1, the $\eta_{OH}$ decreased by 0.16E-4 $cm^3$ in Case 3, which was one order of magnitude less than the decrease of $\eta_{C4H2}$ 0.21E-3 $cm^3$ (see Fig. 15(d)) and $\eta_H$ 0.29E-3 $cm^3$ (see Fig. 15(i)). The larger decreases of $\eta_{C4H2}$ and $\eta_H$ resulted in the drop of $\delta R731$ and $\delta R691$, leading to more A2R5 converted to A2 via R829, consequently increasing $\eta_{A2}$. Though more A2R5 was converted to A2R5- via R692, $\delta R783$ was not increased in the $CO_2$-O, due to the less A1 generated via R497 (i-$C_4H_5$ + $C_2H_2$ = A1 + H) and R489 (2$C_3H_3$ = A1) in Case 3.

As shown in Fig. 14, the $C_4H_2$ was primarily formed via the formation pathway of $C_2H_4 \rightarrow C_2H_3 \rightarrow C_2H_2 \rightarrow C_4H_2$, where R239 ($C_2H_4$ + H = $C_2H_3$ + $H_2$) and R240 ($C_2H_4$ + OH = $C_2H_3$ + $H_2O$) were initial reactions. Compared with Case 1, the $\delta R239$ in Case 3 decreased but the $\delta R240$ increased, due to the larger decline of $\eta_{OH}$ than $\eta_H$. Since the increase of $\delta R240$ was less than the drop of $\delta R239$, the consumption rate of $C_2H_4$ generally decreased, leading to the increase of $\eta_{C2H4}$ in Case 3 shown in Fig. 15(g). Although less $C_2H_4$ was converted to $C_2H_3$, the $\eta_{C2H3}$ increased in Case 3, which was mainly attributed to the larger decline of consumption rate of $C_2H_3$ (R77: $C_2H_2$ + H (+M) = $C_2H_3$ (+M)). Similarly, compared with the formation rate, the decline of the consumption rate of $C_2H_2$ was larger, resulting in the increase of $\eta_{C2H2}$ in Case 3.

While for $C_4H_2$, its consumption rate (R101: $C_4H_2$ + OH = $C_3H_2$ + HCO) decreased more than the formation rate (R81: $C_2H_2$ + $C_2H$ = $C_4H_2$ + H), which was the primary reason for the decline of $\eta_{C4H2}$ in Case 3 shown in Fig. 15(d).

### 3.5. Effect on the soot surface growth

The $\beta_{CO}$ and $\beta_{HACA}$ calculated in Cases 1 ~ 4 were depicted in Fig. 16. The effects of different $CO_2$ addition ways on the peak $\alpha$s shown in Fig. 10(b) and (c) were identical to the $\beta$s shown in Fig. 16(a) and (b). This confirmed that the effects of different $CO_2$ addition on HACA surface growth and condensation processes could be quantitatively evaluated by the peak $\alpha$s.

As indicated in Fig. 16(a) and (b), unlike the soot inception (see Fig. 11), the suppression effects of $CO_2$ addition ways on soot condensation and HACA surface growth were in the order: $CO_2$-F < $CO_2$-O < $CO_2$-F/O. Whereas, the influence extent of $CO_2$ addition ways on soot condensation and HACA surface growth was different. The $CO_2$-F caused the $\beta_{HACA}$ decreasing from 2.66E to 4 g/s to 2.61E-4 g/s, with a drop of 1.9%, which was less than the decrease of $\beta_{CO}$ (by 7%). In the $CO_2$-O, the $\beta_{HACA}$ decreased by 19.9%, which was larger than the decrease of $\beta_{CO}$ (8.8%). The $\beta_{HACA}$ and $\beta_{CO}$ in Case 4 were 21.1% and 14.2% less than those in Case 1, indicating that the $CO_2$-F/O had the most significant inhibiting effect on HACA surface growth and soot condensation.

The soot condensation rate depended on the concentrations of soot and A5s [25]. As shown in Fig. 12, compared with $\gamma_{BGHIF}$, the distributions of $\gamma_{BAPYR}$ were more consistent with those of $\alpha_{CO}$ shown in Fig. 10 (b), implying that BAPYR played a more significant role in the soot
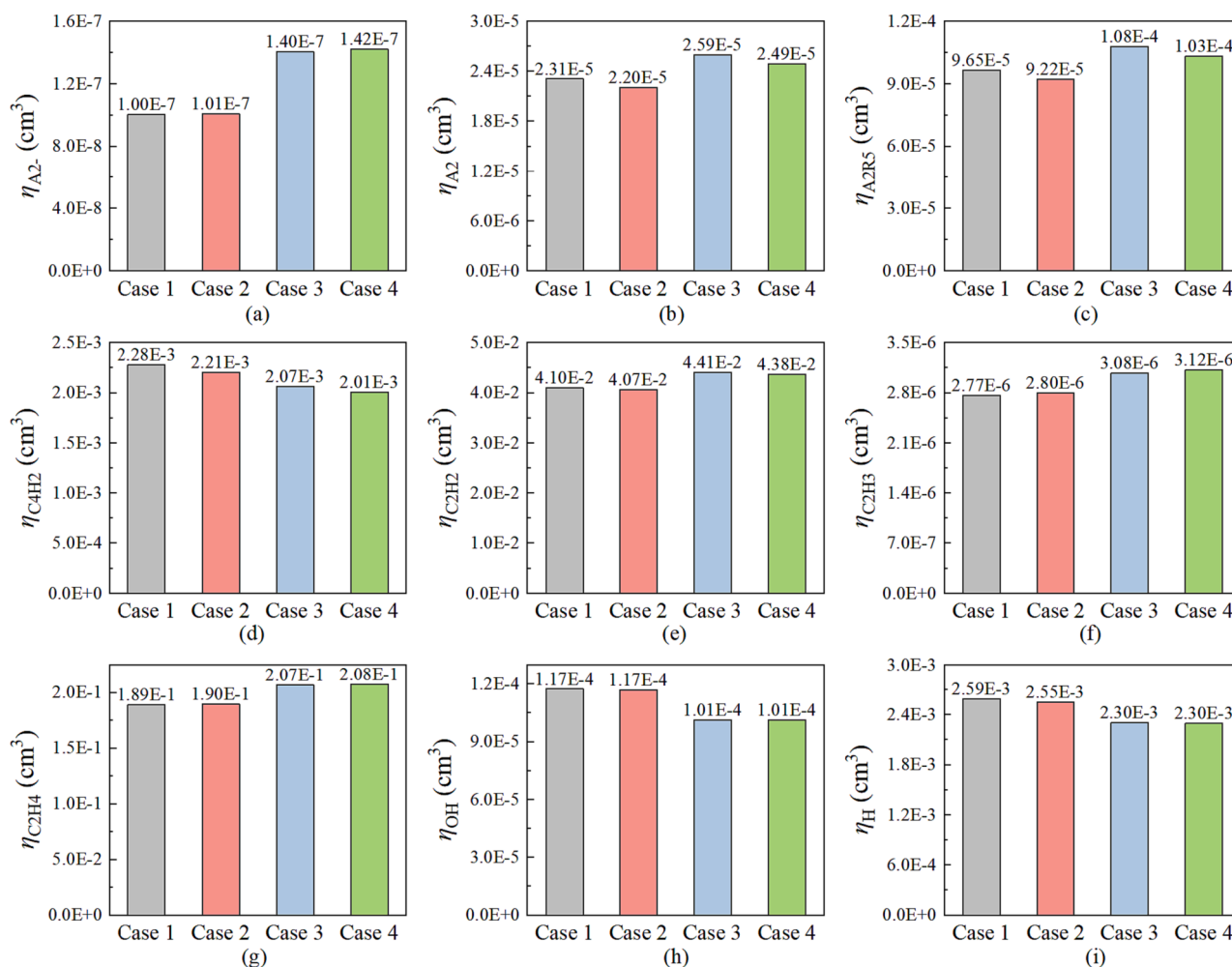
**Fig. 15.** The integrated mole fractions of (a) A2-, (b) A2, (c) A2R5, (d) $C_4H_2$, (e) $C_2H_2$, (f) $C_2H_3$, (g) $C_2H_4$, (h), OH and (i) H over the whole computational domain.
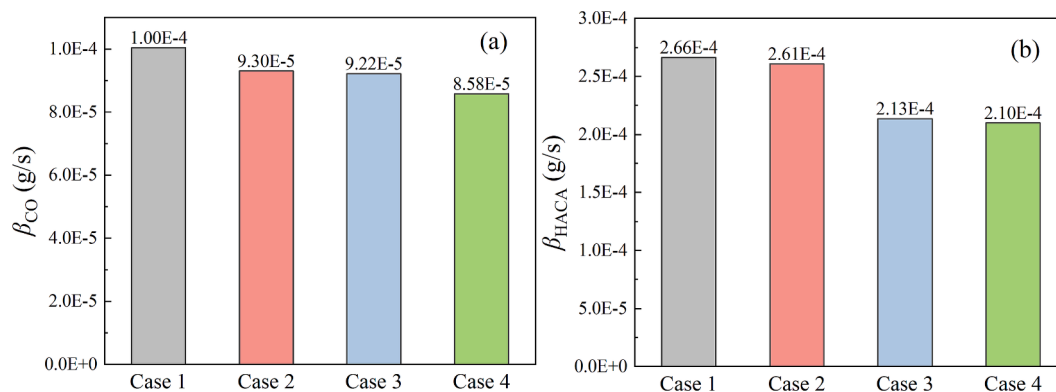


**Fig. 16.** The integrated (a) soot condensation and (b) HACA surface growth rates over the whole computational domain.

condensation process. The formation pathways of BAPYR in Cases 1–4 were compared in Fig. 14.

As shown in Fig. 14, the BAPYR was mainly formed through R781 (A2R5-+A1C2H = BAPYR + H) and R792 ($C_4H_2$ + A4=>BAPYR). Both $\delta$R781 and $\delta$R792 were inhibited in the $CO_2$-F, and the $\delta$R792 decreased more evidently, indicating that R792 was mainly accounted for the decrease of $\gamma_{BAPYR}$ in Case 1. As shown in Fig. 14, the $CO_2$-O had little effect on the $\delta$R781, but a more significant suppression effect on the $\delta$R792. Compared with Case 1, $\delta$R792 decreased by 2.91E-8 mol/s in Case 4, which was obviously larger than the decrease of $\delta$R781 (by

0.37E-8 mol/s). In general, R792 dominated the decrease of $\gamma_{BAPYR}$ in Cases 2–4. As discussed in the previous section, the consumption rate of A2R5 via R731 was inhibited due to the decrease of $\eta_{C4H2}$ in Cases 2 ~ 4, leading to a lower mole fraction of A4, consequently decreasing $\delta$R792.

As shown in Fig. 12, in Cases 2 ~ 4, the peak mole fractions of BAPYR decreased by 6.6%, 12.2% and 17.7%, respectively, while the peak condensation rates shown in Fig. 10(b) decreased by 10.7%, 25.0% and 32.4%, respectively. The decreases of peak condensation rates were almost twice larger than the decreases of peak mole fractions of BAPYR in Cases 2–4, which was due to the decreases of flame temperature and
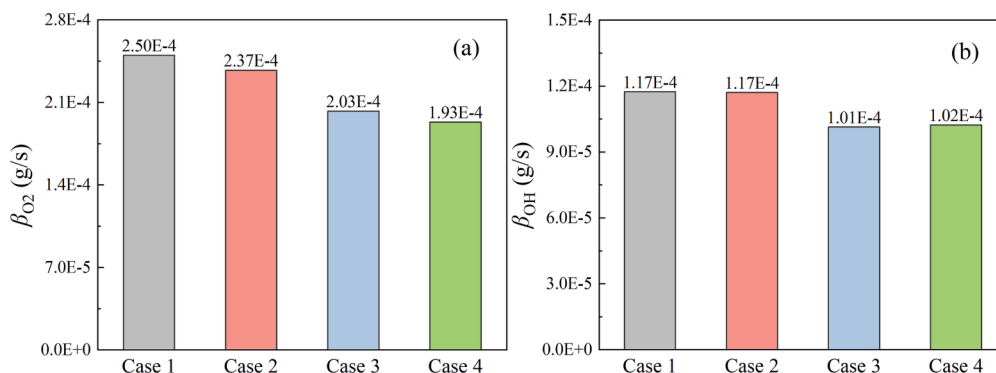
**Fig. 17.** The integrated soot oxidation via (a) $O_2$ and (b) OH rates over the whole computational domain.
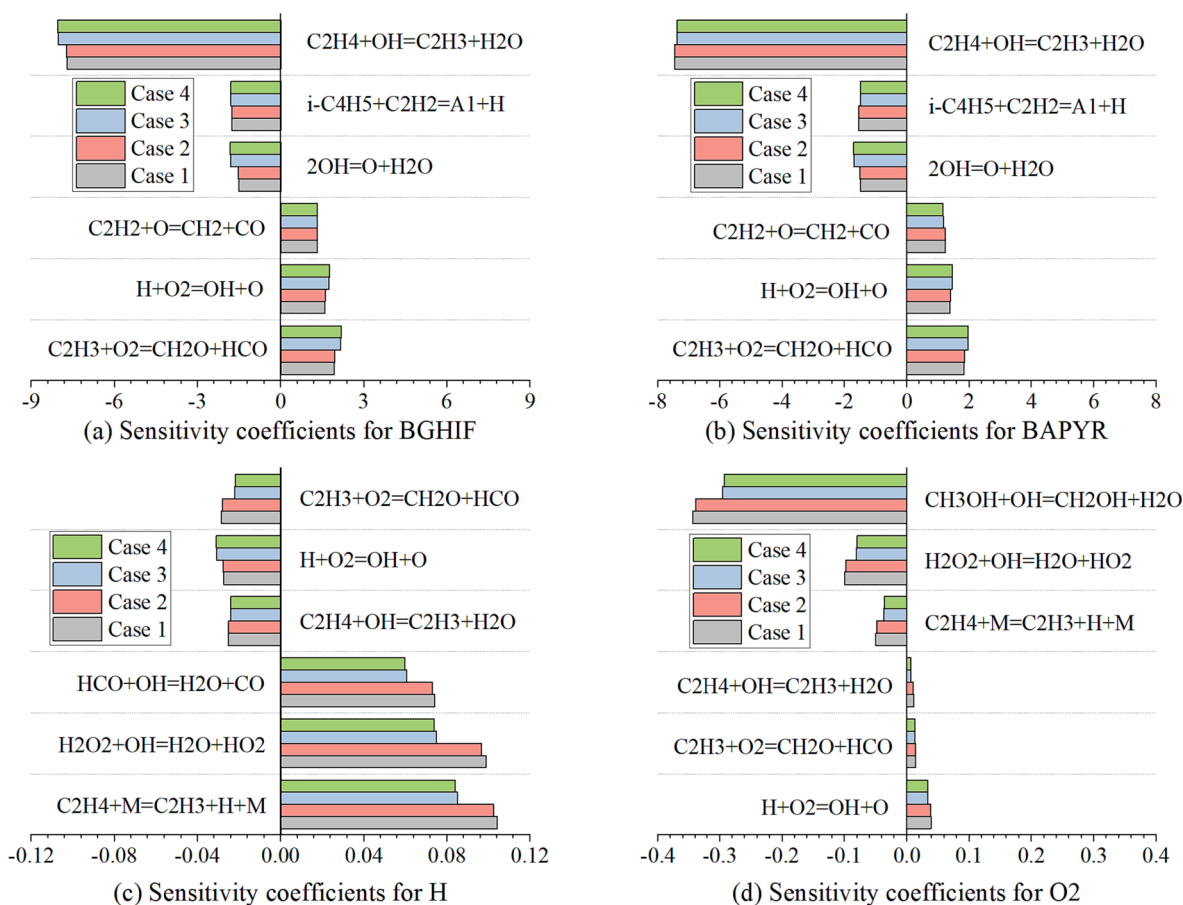


**Fig. 18.** The sensitivity analysis of (a) BGHIF, (b) BAPYR, (c) H and (d) $O_2$.

soot nucleation rate.

As shown in Fig. 16(b), since the suppression effects of the $CO_2$-O and $CO_2$-F/O on the HACA surface growth rate were similar, the following discussion mainly focused on the analysis of the decrease of $\beta_{HACA}$ caused by the $CO_2$-O. The HACA surface growth rate was positively related to the mole fractions of $C_2H_2$, OH and H radicals [25]. As shown in Fig. 15(e), the $\eta_{C2H2}$ increased from 4.1E to 2 mol/s in Case 1 to 4.4E-2 mol/s in Case 3, which was contrary to the change of $\beta_{HACA}$. While the $\eta_H$ and $\eta_{OH}$ showed in Fig. 15(h) and (i) decreased by 13.7% and 11.25% in Case 3, around twice larger than the decrease of $\eta_{C2H2}$ (by 6.8%), which accounted for the decrease of $\beta_{HACA}$ in Case 3. In addition, as mentioned above, the soot condensation process occurred earlier and provided the initial soot for the HACA surface growth process. The $\beta_{CO}$ was limited by the $CO_2$-O, which was another key factor for the decrease

of $\beta_{HACA}$.

### 3.6. Effect on the soot oxidation

The effects of different ways of $CO_2$ addition on the $\beta_{O2}$ and $\beta_{OH}$ were plotted in Fig. 17(a) and (b). In Fig. 17(a), the $\beta_{O2}$ decreased by 5.2% with $CO_2$-F, which was obviously less than those with the $CO_2$-O (by 19.2%) and the $CO_2$-F/O (by 22.8%), owing to the lower $O_2$ concentration in the oxidizer stream in Cases 3 and 4. As shown in Fig. 15(h), there was little discrepancy in $\eta_{OH}$ between Cases 1 and 2, leading to the almost overlap of $\alpha_{OH}$ shown in Fig. 10(e). In addition, both the $CO_2$-O and $CO_2$-F/O resulted in a decrease of $\beta_{OH}$ by 13.7%, which were obviously less than the decrease of $\beta_{O2}$ in Cases 3 and 4. In general, the soot oxidation by $O_2$ process was more sensitive than the soot oxidation

by OH process with the $CO_2$ addition, whichever $CO_2$ addition ways were adopted.

### 3.7. Sensitivity analysis

The sensitivity results of BGHIF, BAPYR, H and $O_2$, which were dominant factors affecting the soot inception, soot condensation, HACA surface growth and soot oxidation by $O_2$ processes, were shown in Fig. 18. As shown in Fig. 18(a) and (b), the three most sensitive reactions for promoting or inhibiting BGHIF and BAPYR in Cases 1–4 were the same. $C_2H_4 + OH = C_2H_3 + H_2O$ was the most sensitive reaction for inhibiting BGHIF and BAPYR. Compared with Case 1, the sensitivity coefficient of $C_2H_4 + OH = C_2H_3 + H_2O$ for BGHIF increased slightly in Cases 3 and 4, but decreased for BAPYR. $C_2H_3 + O_2 = CH_2O + HCO$ was the most sensitive reaction for promoting BGHIF and BAPYR, and its sensitivity coefficient increased when the $CO_2$ was added to the oxidizer stream. It can be seen from Fig. 18(c) that $C_2H_3 + O_2 = CH_2O + HCO$ and $H + O_2 = OH + O$ were the two most sensitive reactions for inhibiting H in Cases 1–4. The sensitivity coefficient of $C_2H_3 + O_2 = CH_2O + HCO$ in case 4 decreased by 23.8% in comparison of case 1, while that of $H + O_2 = OH + O$ increased by 13.2%. $C_2H_4 + M = C_2H_3 + H + M$, $H_2O_2 + OH = H_2O + HO_2$ and $HCO + OH = H_2O + CO$ were three most important reactions for promoting the formation of H. Compared with case 1, all their sensitivity coefficients obviously decreased in cases 3 and 4. As shown in Fig. 18(d), the most controlling reaction for $O_2$ consumption was $CH_3 + OH = CH_2 + H_2O$. The $CO_2$-O and $CO_2$-F/O resulted in the decrease of the sensitivity coefficient of $CH_3 + OH = CH_2 + H_2O$ by 14.2% and 15.0%, respectively.

## 4. Conclusions

The effects of $CO_2$ addition to the fuel, oxidizer and fuel/oxidizer streams on soot formation in a co-flow diffusion ethylene flame were experimentally investigated and compared in this study. The two-dimensional distributions of SVF and flame temperature were reconstructed by using Abel inverse method. The simulations of four different $C_2H_4/CO_2$ flames were performed with detailed gas reaction and soot formation mechanisms to illustrate the experimental results. To further reveal how $CO_2$ addition ways affected the soot formation, the effects of different $CO_2$ addition ways on the soot inception, soot condensation, HACA surface growth, and oxidation by $O_2$/OH processes were quantitatively determined by introducing the integrated reaction rates over the whole computational domain. The main conclusions were as follows.

1) All three $CO_2$ addition ways showed suppression effects on flame temperature and SVF, among which the $CO_2$-F/O was the most effective, followed by the $CO_2$-O, and the $CO_2$-F was the weakest.
2) Compared with the $CO_2$-F, the suppression effect of the $CO_2$-O on soot inception was weaker due to the higher mole fraction of BGHIF. The reason was that the rate of $C_4H_2$ formation via $C_2H_4 \rightarrow C_2H_3 \rightarrow C_2H_2 \rightarrow C_4H_2$ was inhibited by the $CO_2$-O, lowering the consumption rate of A2R5 ($C_4H_2 + A2R5 \Rightarrow A4$), consequently more A2R5 was converted to BGHIF via A2R5 $\rightarrow$ A2- $\rightarrow$ A2 $\rightarrow$ BGHIF. The $CO_2$-F/O had the most significant inhibiting effect on soot inception because of the largest drop of temperature.
3) The suppression effects of different $CO_2$ addition ways on soot condensation and HACA surface growth were identical: $CO_2$-F < $CO_2$-O < $CO_2$-F/O. The decrease of the BAPYR mole fraction accounted for the decrease of soot condensation rates, and the decline of H and OH mole fractions accounted for the drop of HACA surface growth rates. Compared with the $CO_2$-O and $CO_2$-F/O, the $CO_2$-F had the stronger inhibiting effect on the soot condensation, but weaker on the HACA surface growth.
4) Compared with the $CO_2$-F, the $CO_2$-O and $CO_2$-F/O had the stronger suppression effect on the soot oxidation by $O_2$ process due to the lower $O_2$ concentration in the oxidizer stream. Whichever $CO_2$

addition ways were adopted, the soot oxidation by $O_2$ process was more sensitive than the soot oxidation by OH process with the $CO_2$ addition.
5) The sensitivity analysis showed that $C_2H_4 + OH = C_2H_3 + H_2O$ was the most sensitive reaction for inhibiting BGHIF and BAPYR. The $CO_2$-O and $CO_2$-F/O obviously increased the sensitive coefficients of the three most important reactions for promoting the formation of H.

## CRediT authorship contribution statement

**Yu Yang:** Conceptualization, Writing – original draft. **Shu Zheng:** Conceptualization, Visualization, Supervision. **Yuzhen He:** Validation, Visualization. **Hao Liu:** Methodology. **Ran Sui:** Writing – review & editing, Formal analysis. **Qiang Lu:** Conceptualization, Project administration.

## Declaration of Competing Interest

The authors declare that they have no known competing financial interests or personal relationships that could have appeared to influence the work reported in this paper.

## Data availability

Data will be made available on request.

## Acknowledgements

## Appendix A. Supplementary data

Supplementary data to this article can be found online at https://doi.org/10.1016/j.fuel.2023.129181.

## References

[1] Li T, Mitra T, Chu C, Yuan Y, Thomson MJ. Investigation of PAH and soot formation in a dimethyl ether (DME) laminar coflow diffusion flame. Combust Flame 2021;223:437–49.
[2] Tollefson J. Soot a major contributor to climate change. Nature News 2013;15.
[3] Al-Qurashi K, Lueking AD, Boehman AL. The deconvolution of the thermal, dilution, and chemical effects of exhaust gas recirculation (EGR) on the reactivity of engine and flame soot. Combust Flame 2011;158(9):1696–704.
[4] Sui R, Liang W, Zhang L, Mantzaras J, Law CK. Kinetic interactions between H2 and CO in catalytic oxidation over PdO. Combust Flame 2020;211:270–80.
[5] Angrill O, Geitlinger H, Streibel T, Suntz R, Bockhorn H. Influence of exhaust gas recirculation on soot formation in diffusion flames. Proc Combust Inst 2000;28(2):2643–9.
[6] Du DX, Axelbaum RL, Law CK. The influence of carbon dioxide and oxygen as additives on soot formation in diffusion flames. Symp (Int) Combust 1991;23(1):1501–7.
[7] Liu F, Guo H, Smallwood GJ, Gülder ÖL. The chemical effects of carbon dioxide as an additive in an ethylene diffusion flame: implications for soot and NOx formation. Combust Flame 2001;125(1-2):778–87.
[8] Oh KC, Shin HD. The effect of oxygen and carbon dioxide concentration on soot formation in non-premixed flames. Fuel 2006;85(5–6):615–24.
[9] Wang Y, Chung SH. Formation of soot in counterflow diffusion flames with carbon dioxide dilution. Combust Sci Technol 2016;188(4–5):805–17.
[10] Gu M, Chu H, Liu F. Effects of simultaneous hydrogen enrichment and carbon dioxide dilution of fuel on soot formation in an axisymmetric coflow laminar ethylene/air diffusion flame. Combust Flame 2016;166:216–28.
[11] Wu J, Chen L, Bengtsson P-E, Zhou J, Zhang J, Wu X, et al. Effects of carbon dioxide addition to fuel on soot evolution in ethylene and propane diffusion flames. Combust Flame 2019;199:85–95.
[12] Guo H, Smallwood GJ. A numerical study on the influence of CO2 addition on soot formation in an ethylene/air diffusion flame. Combust Sci Technol 2008;180(10–11):1695–708.
[13] Hoerlle CA, Pereira FM. Effects of CO2 addition on soot formation of ethylene non-premixed flames under oxygen enriched atmospheres. Combust Flame 2019;203:407–23.

[14] Ashraf A, Ahmed H, Steinmetz S, Dunn MJ, Masri AR. On the Effects of Carbon Dioxide as a Diluent on Precursor Nanoparticles and Soot in Axi-symmetric Laminar Coflow Diffusion Flames. Combust Sci Technol 2022;194(5):946–62.

[15] Gülder ÖL, Snelling DR, Sawchuk RA. Influence of hydrogen addition to fuel on temperature field and soot formation in diffusion flames. Symp (Int) Combust 1996;26(2):2351–8.

[16] Huang Q-X, Wang F, Liu D, Ma Z-y, Yan J-H, Chi Y, et al. Reconstruction of soot temperature and volume fraction profiles of an asymmetric flame using stereoscopic tomography. Combust Flame 2009;156(3):565–73.

[17] Legros G, Wang Q, Bonnety J, Kashif M, Morin C, Consalvi J-L, et al. Simultaneous soot temperature and volume fraction measurements in axis-symmetric flames by a two-dimensional modulated absorption/emission technique. Combust Flame 2015; 162(6):2705–19.

[18] Eaves NA, Zhang Q, Liu F, Guo H, Dworkin SB, Thomson MJ. CoFlame: A refined and validated numerical algorithm for modeling sooting laminar coflow diffusion flames. Comput Phys Commun 2016;207:464–77.

[19] Chernov V, Thomson MJ, Dworkin SB, Slavinskaya NA, Riedel U. Soot formation with C1 and C2 fuels using an improved chemical mechanism for PAH growth. Combust Flame 2014;161(2):592–601.

[20] Liu F, Dworkin SB, Thomson MJ, Smallwood GJ. Modeling DME addition effects to fuel on PAH and soot in laminar coflow ethylene/air diffusion flames using two PAH mechanisms. Combust Sci Technol 2012;184(7-8):966–79.

[21] Liu F, Becker H, Pollard A. Spatial differencing schemes of the discrete-ordinates method. Numerical Heat Transfer 1996;30(1):23–43.

[22] Liu F, Smallwood GJ, Gülder ÖL. Application of the statistical narrow-band correlated-k method to low-resolution spectral intensity and radiative heat transfer calculations—effects of the quadrature scheme. Int J Heat Mass Transf 2000;43 (17):3119–35.

[23] Lou C, Li Z, Zhang Y, Kumfer BM. Soot formation characteristics in laminar coflow flames with application to oxy-combustion. Combust Flame 2021;227:371–83.

[24] Dworkin SB, Zhang Q, Thomson MJ, Slavinskaya NA, Riedel U. Application of an enhanced PAH growth model to soot formation in a laminar coflow ethylene/air diffusion flame. Combust Flame 2011;158(9):1682–95.

[25] Jerez A, Consalvi J-L, Fuentes A, Liu F, Demarco R. Soot production modeling in a laminar coflow ethylene diffusion flame at different Oxygen Indices using a PAH-based sectional model. Fuel 2018;231:404–16.